CRYSTAL GROWTH & DESIGN

Article

Cite This: *Cryst. Growth Des.* 2018, 18, 1136−1146

pubs.acs.org/crystal

Structural Diversity and Sensing Properties of Metal−Organic Frameworks with Multicarboxylate and 1*H*-Imidazol-4-yl-Containing Ligands

Zhi-Qiang Liu,[†,‡] Kai Chen,[†] Yue Zhao,[†] Yan-Shang Kang,[†] Xiao-Hui Liu,[†] Qing-Yi Lu,[†] Mohammad Azam,[§] Saud I. Al-Resayes,[§] and Wei-Yin Sun*[,†]

[†]Coordination Chemistry Institute, State Key Laboratory of Coordination Chemistry, School of Chemistry and Chemical Engineering, Nanjing National Laboratory of Microstructures, Collaborative Innovation Center of Advanced Microstructures, Nanjing University, Nanjing 210023, China

[‡]School of Chemistry and Chemical Engineering, Anhui Province Key Laboratory of Functional Optical, Electrical and Magnetic Materials, Key Laboratory of Functional Coordination Compounds and Nano Materials of Anhui Higher Education Institutes, Anqing Normal University, Anqing 246011, China

[§]Department of Chemistry, College of Science, King Saud University, P.O. Box 2455, Riyadh 11451, Kingdom of Saudi Arabia

S *Supporting Information*

ABSTRACT: Two 1*H*-imidazol-4-yl-containing ligands 1,3-di(1*H*-imidazol-4-yl)benzene (L^1) and 4,4′-di(1*H*-imidazol-4-yl)biphenyl (L^2) were employed to react with corresponding metal salt together with varied carboxylate ligands under hydro- and solvothermal conditions, and six new metal−organic frameworks (MOFs) $[Cd(L^1)(oba)]\cdot DMF$ (**1**), $[Ni_3(L^1)_2(BPT)_2(H_2O)_4]$ (**2**), $[Zn_2(L^1)_2(HBPT)_2]\cdot H_2O$ (**3**), $[Ni(L^1)(BPTC)_{0.5}(H_2O)_2]$ (**4**), $[Ni_2(\mu_2\text{-}O)(L^2)_3(Hoba)_2(H_2O)_2]$ (**5**), and $[Ni_2(L^2)_3(BPTC)(H_2O)_2]\cdot 6H_2O$ (**6**) [H_2oba = 4,4′-oxybis(benzoic acid), H_3BPT = biphenyl-3,4′,5-tricarboxylic acid, H_4BPTC = biphenyl-3,3′,5,5′-tetracarboxylic acid, DMF = *N*,*N*-dimethylformamide] were achieved and structurally characterized. MOFs **1**, **3**, **4**, and **5** are different two-dimensional networks, which are further joined together by hydrogen bonds to generate three-dimensional (3D) supramolecular frameworks. **2** is a (4,4)-connected binodal 3D framework with a point symbol of $\{3\cdot4\cdot5\cdot8^3\}_4\{3^2\cdot8^2\cdot9^2\}$, while **6** is a diamond 3D framework. The results show that coordination geometry of the metal centers and coordination mode of the ligands play important roles in the formation of MOFs with diverse structures. Moreover, luminescent studies showed that **1** and **3** represent highly efficient quenching for detecting Fe^{3+} ions and acetone molecules. In addition, **6** exhibits selectively adsorption of CO_2 over N_2.

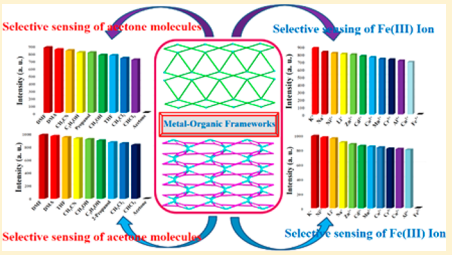

INTRODUCTION

Metal−organic frameworks (MOFs), as a new type of organic−inorganic hybrid material, have characteristic features of both metal centers and organic linkers, and resulting in a wide variety of potential applications in the fields such as chemical sensing, gas adsorption and separation, energy storage and conversion, catalysis, drug delivery, and so on.[1−6] Among the reported MOFs, studies on the luminescent properties of MOFs are especially interesting for researchers, and over the past few years, various luminescent MOFs (LMOFs) have been synthesized not only as luminescent materials, but also as fluorescent sensors for the detection of solvent and small organic molecules, specific metal ions, and anions.[7−11] However, at the present stage, fabrication of MOFs with definite framework structures and specific properties in a designable and controllable manner is still a challenge. Further and systematic studies are required for the design and synthesis of MOFs that can recognize and sense definite molecules and/or ions.

We focused our attention on the design and synthesis of MOFs with varied multicarboxylate and imidazol-containing ligands and found that they show diverse framework structures and interesting properties including LMOFs for sensing application.[12−15] In this work, we report on six new MOFs $[Cd(L^1)(oba)]\cdot DMF$ (**1**), $[Ni_3(L^1)_2(BPT)_2(H_2O)_4]$ (**2**), $[Zn_2(L^1)_2(HBPT)_2]\cdot H_2O$ (**3**), $[Ni(L^1)(BPTC)_{0.5}(H_2O)_2]$ (**4**), $[Ni_2(\mu_2\text{-}O)(L^2)_3(Hoba)_2(H_2O)_2]$ (**5**), and $[Ni_2(L^2)_3(BPTC)(H_2O)_2]\cdot 6H_2O$ (**6**) (DMF = *N*,*N*-dimethylformamide) constructed by corresponding metal salt with varied carboxylate ligands 4,4′-oxybis(benzoic acid) (H_2oba), biphenyl-3,4′,5-tricarboxylic acid (H_3BPT) as well as biphenyl-3,3′,5,5′-tetracarboxylic acid (H_4BPTC) and 1*H*-imidazol-4-yl containing ligands 1,3-di(1*H*-imidazol-4-yl)benzene (L^1) and 4,4′-di(1*H*-imidazol-4-yl)-biphenyl (L^2). Luminescence studies reveal that MOFs **1** and **3** are multiresponsive luminescent probes for detecting acetone molecules and Fe^{3+} ions. In addition, **6** exhibits selectively adsorption of CO_2 over N_2.

Received: November 10, 2017
Revised: December 7, 2017
Published: December 28, 2017

DOI: 10.1021/acs.cgd.7b01572
Cryst. Growth Des. 2018, 18, 1136−1146

EXPERIMENTAL SECTION

Synthesis of [Cd(L^1)(oba)]·DMF (1). A mixture of L^1 (21.0 mg, 0.1 mmol), $Cd(NO_3)_2·4H_2O$ (61.6 mg, 0.2 mmol), and H_2oba (25.8 mg, 0.1 mmol) in DMF/H_2O (10 mL, v/v, 1:3) was sealed in a Teflon-lined stainless steel container and heated at 120 °C for 3 days. After being cooled to room temperature, colorless block crystals of **1** were obtained in 88% yield based on L^1. Anal. Calcd for $C_{29}H_{25}N_5O_6Cd$: C, 53.43; H, 3.87; N, 10.74%. Found: C, 53.56; H, 3.76; N, 10.82%. IR (KBr pellet, cm^{-1}): 3137(m), 1650(s), 1598(s), 1526(s), 1383 (s), 1237(w), 1132(w), 1014(w), 952(w), 827(m), 791(s), 744(m), 690(w), 645(w), 520(w).

Synthesis of [Ni$_3$(L^1)$_2$(BPT)$_2$(H$_2$O)$_4$] (2). A mixture of L^1 (21.0 mg, 0.10 mmol), $Ni(NO_3)_2·6H_2O$ (58.1 mg, 0.20 mmol), H_3BPT (28.6 mg, 0.1 mmol), and NaOH (12.0 mg, 0.3 mmol) in H_2O (10 mL) was sealed in a Teflon-lined stainless steel container and heated at 120 °C for 3 days. After being cooled to room temperature, green block crystals of **2** were obtained in 72% yield based on L^1. Anal. Calcd for $C_{54}H_{42}N_8O_{16}Ni_3$: C, 52.51; H, 3.43; N, 9.07%. Found: C, 52.41; H, 3.51; N, 9.03%. IR (KBr pellet, cm^{-1}): 3374 (m), 3156 (m), 1632 (s), 1609 (s), 1586 (s), 1527 (m), 1460 (m), 1398 (s), 1368 (s), 1138 (m), 978 (w), 943 (w), 781 (s), 767 (w), 679 (w), 664 (w), 488 (w), 451 (w).

Synthesis of [Zn$_2$(L^1)$_2$(HBPT)$_2$]·H$_2$O (3). **3** was obtained by the same procedure used for preparation of **2**, except that $Zn(NO_3)_2·6H_2O$ (59.6 g, 0.2 mmol) was used instead of $Ni(NO_3)_2·6H_2O$. After being cooled to room temperature, colorless block crystals of **3** were obtained in 56% yield based on L^1. Anal. Calcd for $C_{42}H_{28}N_4O_{13}Zn_2$: C, 54.39; H, 3.04; N, 6.04%. Found: C, 54.29; H, 3.02; N, 6.11%. IR (KBr pellet, cm^{-1}): 3218 (w), 1689 (s), 1606 (s), 1564 (s), 1442 (m), 1412 (m), 1349 (s), 1286 (s), 1181 (m), 1073 (s), 967 (w), 860 (m) 831 (m), 805 (m), 769 (s), 728 (s), 686 (m), 507 (m).

Synthesis of [Ni(L^1)(BPTC)$_{0.5}$(H$_2$O)$_2$] (4). A mixture of L^1 (21.0 mg, 0.10 mmol), $Ni(NO_3)_2·6H_2O$ (58.1 mg, 0.20 mmol), H_4BPTC (16.5 mg, 0.05 mmol), and NaOH (8.0 mg, 0.2 mmol) in H_2O (10 mL) was sealed in a Teflon-lined stainless steel container and heated at 120 °C for 3 days. After being cooled to room temperature, colorless block crystals of **4** were obtained in 52% yield based on L^1. Anal. Calcd for $C_{20}H_{17}N_4O_6Ni$: C, 51.32; H, 3.66; N, 11.97%. Found: C, 51.21; H, 3.53; N, 12.01%. IR (KBr pellet, cm^{-1}): 3450 (m), 3207 (w), 1606 (w), 1548 (m), 1468 (w), 1350 (s), 1306 (m), 1179 (w), 1162 (m), 1141 (w), 1082 (w), 983 (w) 964 (w), 874 (m), 782 (s), 748 (m), 674 (m), 656 (m).

Synthesis of [Ni$_2$(μ_2-O)(L^2)$_3$(Hoba)$_2$(H$_2$O)$_2$] (5). A mixture of L^2 (28.6 mg, 0.10 mmol), $Ni(NO_3)_2·6H_2O$ (58.1 mg, 0.20 mmol), H_2oba (25.8 mg, 0.1 mmol), and NaOH (8.0 mg, 0.2 mmol) in H_2O (10 mL) was sealed in a Teflon-lined stainless steel container and heated at 120 °C for 3 days. After being cooled to room temperature, colorless block crystals of **5** were obtained in 73% yield based on L^2. Anal. Calcd for $C_{82}H_{64}N_{12}O_{13}Ni_2$: C, 63.84; H, 4.18; N, 10.89%. Found: C, 63.69; H, 4.22; N, 10.86%. IR (KBr pellet, cm^{-1}): 3412 (m), 2831 (m), 1596 (s), 1547 (s), 1490 (m), 1378 (s), 1235 (s), 1164 (m), 1124 (m), 1071 (m), 950 (w), 873 (m), 819 (m), 709 (w), 649 (m), 579 (w), 508 (w), 458 (w).

Synthesis of [Ni$_2$(L^2)$_3$(BPTC)(H$_2$O)$_2$]·6H$_2$O (6). **6** was achieved by the same procedure used for preparation of **4**, except that L^2 (28.6 mg, 0.10 mmol) was used instead of L^1. After being cooled to room temperature, colorless block crystals of **5** were obtained in 82% yield based on L^2. Anal. Calcd for $C_{70}H_{64}N_{12}O_{16}Ni_2$: C, 58.11; H, 4.46; N, 11.62%. Found: C, 58.20; H, 4.39; N, 11.53%. IR (KBr pellet, cm^{-1}): 3596 (m), 3132 (m), 1610 (m), 1567 (m), 1532 (s), 1498 (m), 1442 (m), 1395 (m), 1263 (w), 1156 (s), 1070 (m), 829 (s), 784 (s), 730 (s), 656 (s), 536 (w).

RESULTS AND DISCUSSION

MOFs **1**–**6** were isolated by reactions of metal salts with mixed organic ligands in aqueous DMF or NaOH solution at 120 °C for 3 days, their structures were determined by single crystal X-ray diffraction, and the details of the crystal parameters, data collection, and refinements for **1**–**6** are summarized in Table 1.

Table 1. Crystal Data and Structure Refinements for 1–6

	1	2	3
formula	$C_{29}H_{25}N_5O_6Cd$	$C_{54}H_{42}N_8O_{16}Ni_3$	$C_{42}H_{28}N_4O_{13}Zn_2$
formula weight	651.94	1235.08	927.42
crystal system	monoclinic	monoclinic	monoclinic
space group	*I*2/*a*	*P*2$_1$/*c*	*C*2/*c*
a (Å)	15.7983(13)	23.818(5)	57.243(5)
b (Å)	12.4264(10)	15.620(5)	9.554(5)
c (Å)	28.3002(17)	6.655(5)	13.920(5)
α (deg)	90	90	90
β (deg)	101.169(3)	96.064(5)	103.257(5)
γ (deg)	90	90	90
V (Å^3)	5450.6(7)	2462(2)	7410(5)
Z	8	2	8
D_c (g cm^{-3})	1.589	1.666	1.663
M (mm^{-1})	0.855	1.221	1.373
F(000)	2640	1268	3776
reflections collected	18118	13613	20010
unique reflections	6228	4332	6538
goodness-of-fit	1.023	1.117	0.979
R_1[a] [$I > 2\sigma(I)$]	0.0277	0.0309	0.0336
wR_2[b] [$I > 2\sigma(I)$]	0.0701	0.0810	0.0888
	4	**5**	**6**
formula	$C_{20}H_{17}N_4O_6Ni$	$C_{82}H_{64}N_{12}O_{13}Ni_2$	$C_{70}H_{64}N_{12}O_{16}Ni_2$
formula weight	468.08	1542.87	1446.75
crystal system	monoclinic	triclinic	monoclinic
space group	*C*2/*m*	*P*$\bar{1}$	*P*2$_1$/*n*
a (Å)	17.071(2)	12.0660(17)	11.5210(9)
b (Å)	17.390(2)	12.8750(19)	25.859(2)
c (Å)	6.6620(9)	13.903(2)	11.689(1)
α (deg)	90	94.166(2)	90
β (deg)	103.060(2)	111.749(2)	109.931(2)
γ (deg)	90	115.691(2)	90
V (Å^3)	1926.6(4)	1736.1(4)	3273.8(5)
Z	4	1	2
D_c (g cm^{-3})	1.614	1.476	1.468
M (mm^{-1})	1.056	0.621	0.656
F(000)	964	800	1504
reflections collected	12835	22321	18581
unique reflections	1757	7999	5775
goodness-of-fit	1.077	1.015	1.019
R_1[a] [$I > 2\sigma(I)$]	0.0242	0.0395	0.0485
wR_2[b] [$I > 2\sigma(I)$]	0.0686	0.0991	0.1144

[a] $R_1 = \Sigma||F_0| - |F_c||/\Sigma|F_0|$. [b] $wR_2 = |\Sigma w(|F_0|^2 - |F_c|^2)|/\Sigma|w(F_0)^2|^{1/2}$, where $w = 1/[\sigma^2(F_0^2) + (aP)^2 + bP]$. $P = (F_0^2 + 2F_c^2)/3$.

Crystal Structure of [Cd(L^1)(oba)]·DMF (1). As exhibited in Figure 1a, Cd1 in **1** is five-coordinated by two N atoms (N1B, N4) from two distinct L^1 and three carboxylate O ones (O1, O2, O4A) from two different oba^{2-} ligands. The Cd–O bond distances are from 2.2313(19) to 2.4367(17) Å, while the Cd–N ones are 2.2418(18) and 2.3135(19) Å. The coordination angles around Cd(II) in **1** are from 54.23(5) to 144.76(6)° (Table S1). Each L^1 links two Cd(II) to form an infinite one-dimensional (1D) helical chain (Figure 1b), and each oba^{2-} connects two Cd(II) using its two carboxylate groups with (μ_1-η^1: η^1)-(μ_1-η^1: η^0)-oba^{2-} mode to give another 1D helical chain (Figure 1c). Then, two kinds of 1D chains cross-link together to generate a two-dimensional (2D) network of **1** (Figure 1d), which is further extended into a three-dimensional (3D) supramolecular architecture through O–H---O hydrogen bonding interactions (Figure 1e and Table S2).

DOI: 10.1021/acs.cgd.7b01572
Cryst. Growth Des. 2018, 18, 1136–1146

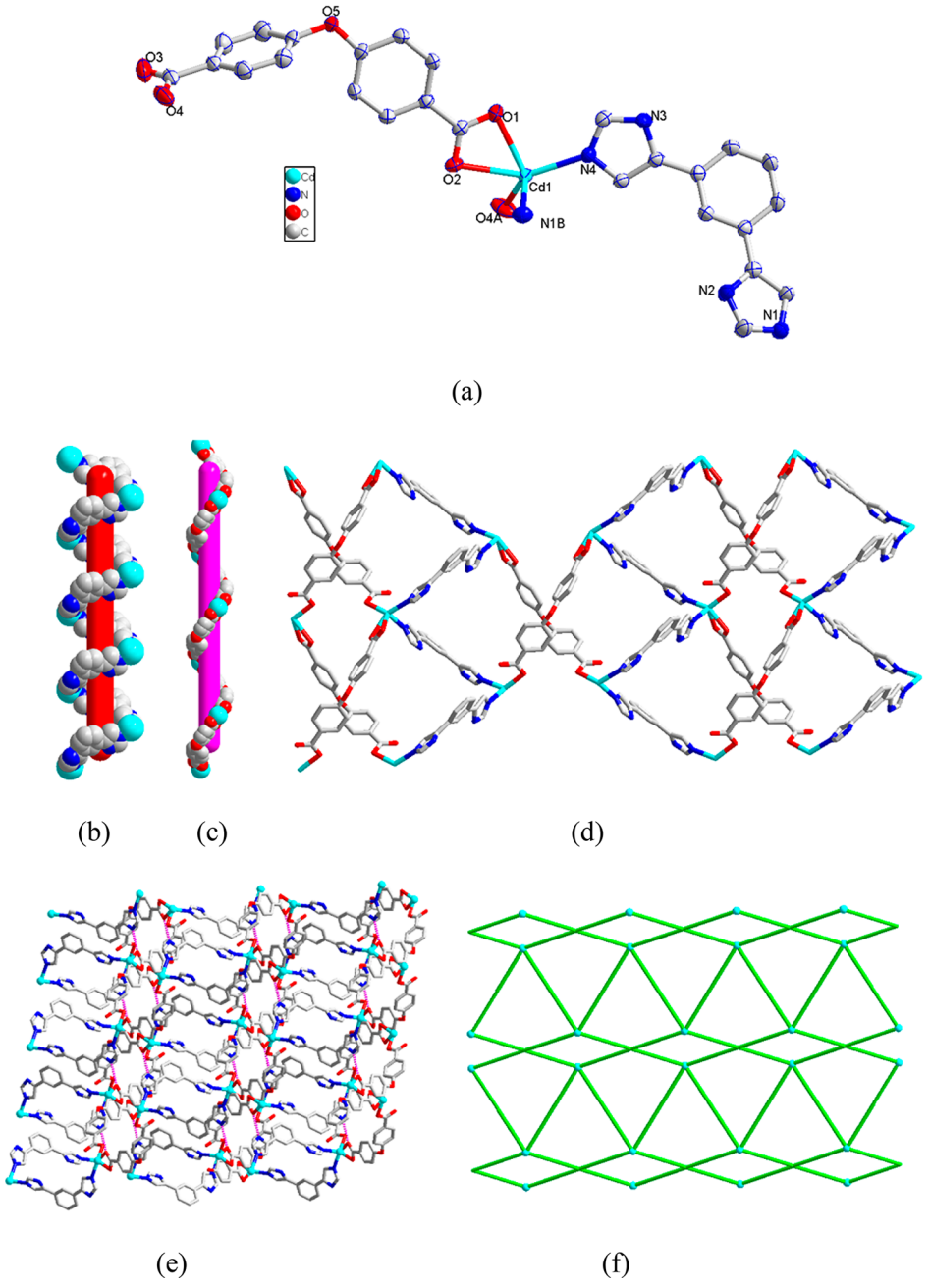

Figure 1. (a) Coordination environment of Cd(II) in **1** with the ellipsoids drawn at the 30% probability level. Hydrogen atoms and DMF molecules are omitted for clarity. (b) Helical chain constructed by Cd(II) and L^1. (c) Helical chain formed by Cd(II) and oba^{2-}. (d) 2D network of **1**. (e) 3D structure of **1** with hydrogen bonds indicated by dashed lines. (f) Topology of **1**.

To simplify the 2D structure of **1**, topological analysis was performed. As shown in Figure 1f, Cd(II), L^1, and oba^{2-} can be regarded as four-, two-, and two-connectors, respectively. Therefore, the resulting structure of **1** is a 4-connected uninodal net with a Schläfli symbol of (6^6) topology calculated by TOPOS program.[16,17]

Crystal Structure of $[Ni_3(L^1)_2(BPT)_2(H_2O)_4]$ (2). The asymmetric unit of **2** has half molecule of $[Ni_3(L^1)_2(BPT)_2(H_2O)_4]$ and contains two Ni(II) atoms, one of which is located at an inversion center, one L^1, one BPT^{3-} and two coordinated water molecules. As exhibited in Figure 2, Ni1 is six-coordinated with octahedral coordination geometry and surrounded by two N atoms (N4B, N4C) from two different L^1, two carboxylate O ones (O5, O5A) from two BPT^{3-}, and two coordinated water molecules (O7, O7A). The Ni1−N bond length is 2.084(2) Å and the Ni1−O ones are 2.0372(17) Å and 2.106(2) Å. In addition, the coordination angles around Ni1 span from 87.60(8) to 180° (Table S1). Ni2 has a N_1O_5 donor set with four carboxylate O atoms (O1, O2, O3D, O4E) from the BPT^{3-} ligand, one imidazole N (N1) from L^1, and one coordinated water molecule (O8). The Ni2−N bond length is 2.022(2) Å, while the Ni2−O ones are in the range of 1.9971(17)−2.232(2) Å. The coordination angles around Ni2 are from 62.62(7) to 169.11(7)° (Table S1). It is noteworthy that each BPT^{3-} in **2** connects four metal atoms using its three carboxylate groups with $(\mu_1\text{-}\eta^1\text{:}\eta^0)\text{-}(\mu_1\text{-}\eta^1\text{:}\eta^1)\text{-}(\mu_2\text{-}\eta^1\text{:}\eta^1)\text{-}BPT^{3-}$ coordination mode (Scheme S1a). Ligands BPT^{3-} link Ni(II) atoms to form a 3D architecture (Figure 2b). Furthermore, L^1 ligands filled into the Ni(II)-BPT 3D net via

DOI: 10.1021/acs.cgd.7b01572
Cryst. Growth Des. 2018, 18, 1136−1146

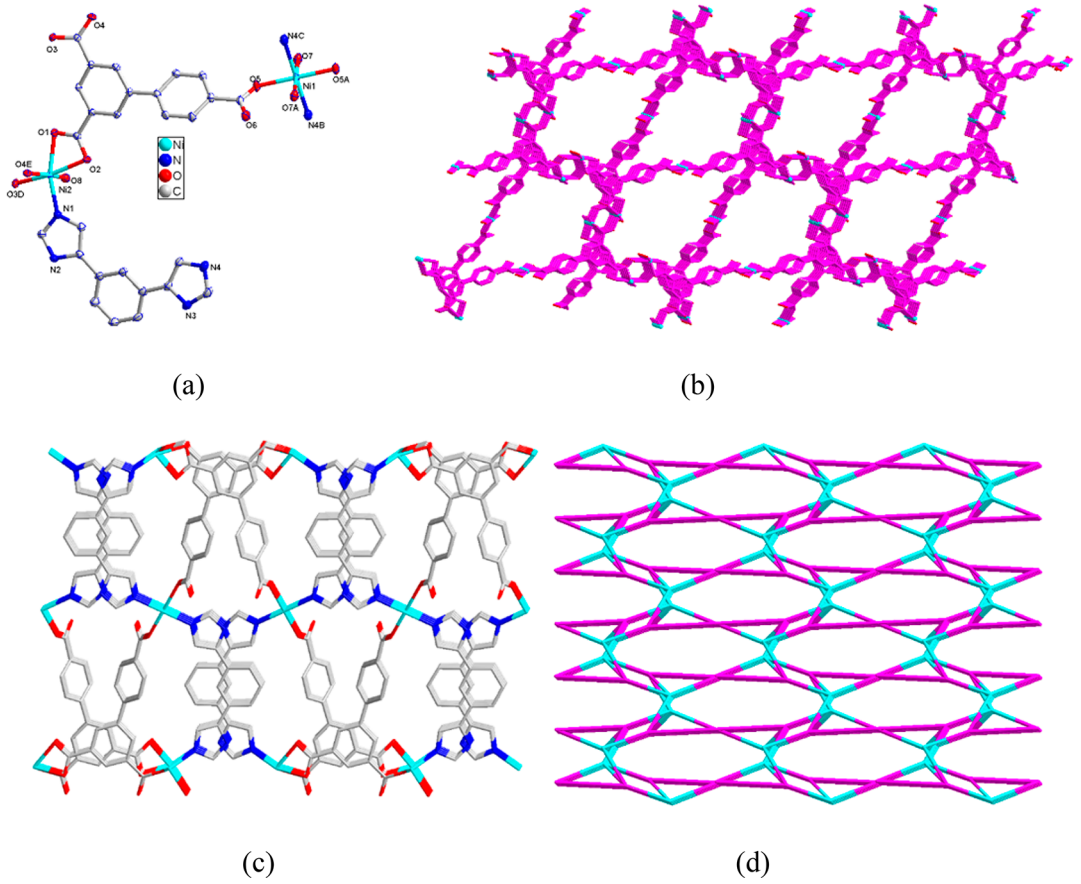

Figure 2. (a) Coordination environment of Ni(II) in **2** with ellipsoids drawn at the 30% probability level. Hydrogen atoms are omitted for clarity. (b) 3D framework of Ni(II)-BPT^{3-}. (c) 3D framework of **2**. (d) Topology of **2**.

Ni−N coordination interactions to give the eventual 3D architecture of **2** (Figure 2c).

Topological analysis was used to get insight into the structure of **2**; each 2-connected bridging L^1 can be regarded as a linear linker. Ni1 and Ni2 atoms can be regarded as 4-connected nodes. Each BPT^{3-} ligand connects four Ni(II) atoms and can be treated as a 4-connector. Therefore, the resulting structure of **2** can be simplified as a (4,4)-connected binodal 3D net, as shown in Figure 2d. The point (Schläfli) symbol for the net is $\{3{\cdot}4{\cdot}5{\cdot}8^3\}_4\{3^2{\cdot}8^2{\cdot}9^2\}$ calculated by TOPOS program.[16,17]

Crystal Structure of $[Zn_2(L^1)_2(HBPT)_2]{\cdot}H_2O$ (3). When $Zn(NO_3)_2{\cdot}6H_2O$ instead of $Ni(NO_3)_2{\cdot}6H_2O$ was used under the same reaction conditions as those for preparation of **2**, complex **3** was isolated. As shown in Figure 3a, both Zn1 and Zn2 are four coordinated with seriously distorted tetrahedral coordination geometry. In addition, the Ni(II) atoms in **2** have N_2O_4 (Ni1) and N_1O_5 (Ni2) coordination environments (Figure 2a), while the Zn(II) atoms in **3** are surrounded by N_1O_3 donor sets (Figure 3a). On the other hand, the $HBPT^{2-}$ adopts a μ_3-bridging mode to connect three metal atoms using its two carboxylate groups with $(\mu_1\text{-}\eta^1{:}\eta^0)\text{-}(\mu_2\text{-}\eta^1{:}\eta^1)$-HBPT coordination mode (Scheme S1b). Ligands $HBPT^{2-}$ link Zn(II) atoms to form a 1D chain (Figure 3b). The Zn(II)-$HBPT^{2-}$ 1D chains are further connected by L^1 ligands to generate a 2D network (Figure 3c), which is further extended into a 3D supramolecular architecture through hydrogen bonding interactions (Figure 3d and Table S2).

Crystal Structure of $[Ni(L^1)(BPTC)_{0.5}(H_2O)_2]$ (4). To further investigate the effect of carboxylate ligand on the structural diversity of the MOFs, H_4BPTC, instead of H_3BPT, was used in the reaction, and MOF **4** with a different structure was successfully obtained. As exhibited in Figure 4a, Ni1 is six-coordinated with octahedral coordination geometry and surrounded by two N atoms (N1, N1A) from two different L^1, two carboxylate O ones (O3, O3C) and two coordinated water molecules (O1W, O1WA). The Ni1−N bond length is 2.0420 (15) Å, while the Ni1−O ones are in the range of 2.0773(12)−2.1282(12) Å. The coordination angles around Ni1 are from 88.26(5) to 180° (Table S1). L^1 ligands link Ni(II) atoms to form an infinite 1D chain (Figure 4b). It is noteworthy that each $BPTC^{4-}$ in **4** connects four metal atoms using its four carboxylate groups with $(\mu_1\text{-}\eta^1{:}\eta^0)\text{-}(\mu_1\text{-}\eta^1{:}\eta^0)\text{-}(\mu_1\text{-}\eta^1{:}\eta^0)\text{-}(\mu_1\text{-}\eta^1{:}\eta^0)$-BPTC coordination mode (Scheme S1c) to form a 2D network (Figure 4c). The Ni(II)-L^1 1D chains are further connected by $BPTC^{4-}$ ligands to generate the final 2D network of **4** (Figure 2d), which is further extend into a 3D supramolecular architecture via O−H---O hydrogen bonding interactions (Figure 4e and Table S2).

Crystal Structure of $[Ni_2(\mu_2\text{-}O)(L^2)_3(Hoba)_2(H_2O)_2]$ (5). As shown in Figure 5a, the Ni1 atom is surrounded by three N atoms from three different L^2, three O ones from one $Hoba^-$ ligand, one μ_2-O, and one coordinated H_2O molecule. The Ni−N bond distances are in the range of 2.0522(16)−2.0880(15) Å, and the Ni1−O ones are from 2.0387(15) to 2.2982(3) Å. In addition, the coordination angles around Ni1 span from 84.25(4) to 177.72(5)° (Table S1). Each L^2 acts as a bridging ligand to connect two Ni(II), at the same time, two Ni1 atoms are connected together via the bridge linking of O5 to form a dinuclear SBU, and Ni1 joins three L^2 ligands to form a 2D network (Figure 5b). It is noteworthy that the $Hoba^-$ acts a

DOI: 10.1021/acs.cgd.7b01572
Cryst. Growth Des. 2018, 18, 1136−1146

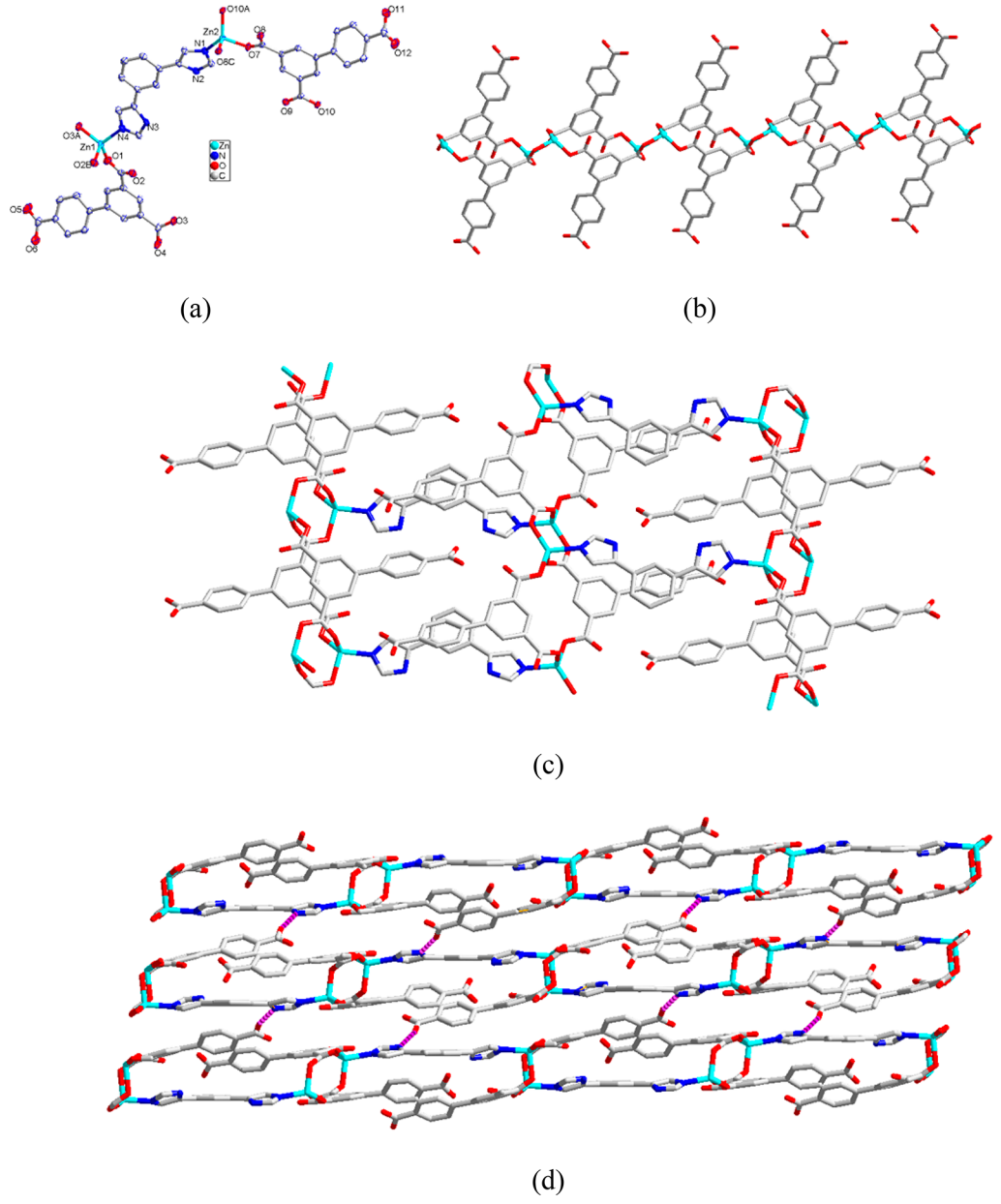

Figure 3. (a) Coordination environment of Zn(II) in **3** with the ellipsoids drawn at the 30% probability level. Hydrogen atoms and free water molecules are omitted for clarity. (b) 1D chains of Zn(II)-$HBPT^{2-}$ in **3**. (c) 2D structure of **3**. (d) 3D structure of **3** with hydrogen bonds indicated by dashed lines.

terminal ligand (Figure 5c). Furthermore, the adjacent 2D networks are further linked together by hydrogen bonds to form a 3D supramolecular framework of **5** (Figure 5d and Table S2).

Crystal Structure of $[Ni_2(L^2)_3(BPTC)(H_2O)_2]\cdot 6H_2O$ (6). When the rigid auxiliary tetracarboxylate ligand H_4BPTC was used instead of the dicarboxylate ligand H_2oba under similar reaction conditions used for fabrication of **5**, framework **6** with entirely different structure was obtained. As exhibited in Figure 6a, Ni1 is six-coordinated by three N atoms (N1, N3A, N5) from three different L^2 ligands, two carboxylate O atoms (O1, O2) from two different $BPTC^{4-}$ ligands, and an additional O (O1W) from coordinated aqua molecule. The Ni−O distances range from 2.109(2) to 2.215(2) Å, and the Ni−N ones are in the range of 2.035(3)−2.075(3) Å. The range of coordination angles around Ni1 is from 60.94(8) to 173.25(10)° (Table S1). Each Ni(II) links three L^2 ligands to form a 2D network (Figure 6b), two of four carboxylate groups of each $BPTC^{4-}$ adopt $(\mu_1\text{-}\eta^1\text{:}\eta^1)$-$(\mu_1\text{-}\eta^1\text{:}\eta^1)$-BPTC coordination mode (Scheme S1d), and as a result, the $BPTC^{4-}$ ligands join the Ni(II)-L^2 2D network to form the final 3D framework structure of **6** (Figure 6c). PLATON calculations suggest that the resulting void volume in **6** is 9.8% occupied by water molecules.

From the view of topology, the Ni(II) atom as a 4-connecting node and L^2, $BPTC^{4-}$ ligands as linkers, the overall structure of **6** is a 5-fold interpenetrated diamond framework (dia net) as illustrated in Figure 6d.

Comparison the Structures of 1−6. The above-mentioned crystallographic results clearly show the diverse structures of **1**−**6** from 2D networks to 3D frameworks, in which the metal centers are four-, five-, and six-coordinated and the carboxylate ligands display varied coordination modes. The different structures of **2** and **3** are ascribed to the distinct metal centers since they were prepared under the same reaction conditions except for the different metal salts. In the Ni(II) complexes, **2** and **4** with

DOI: 10.1021/acs.cgd.7b01572
Cryst. Growth Des. 2018, 18, 1136−1146

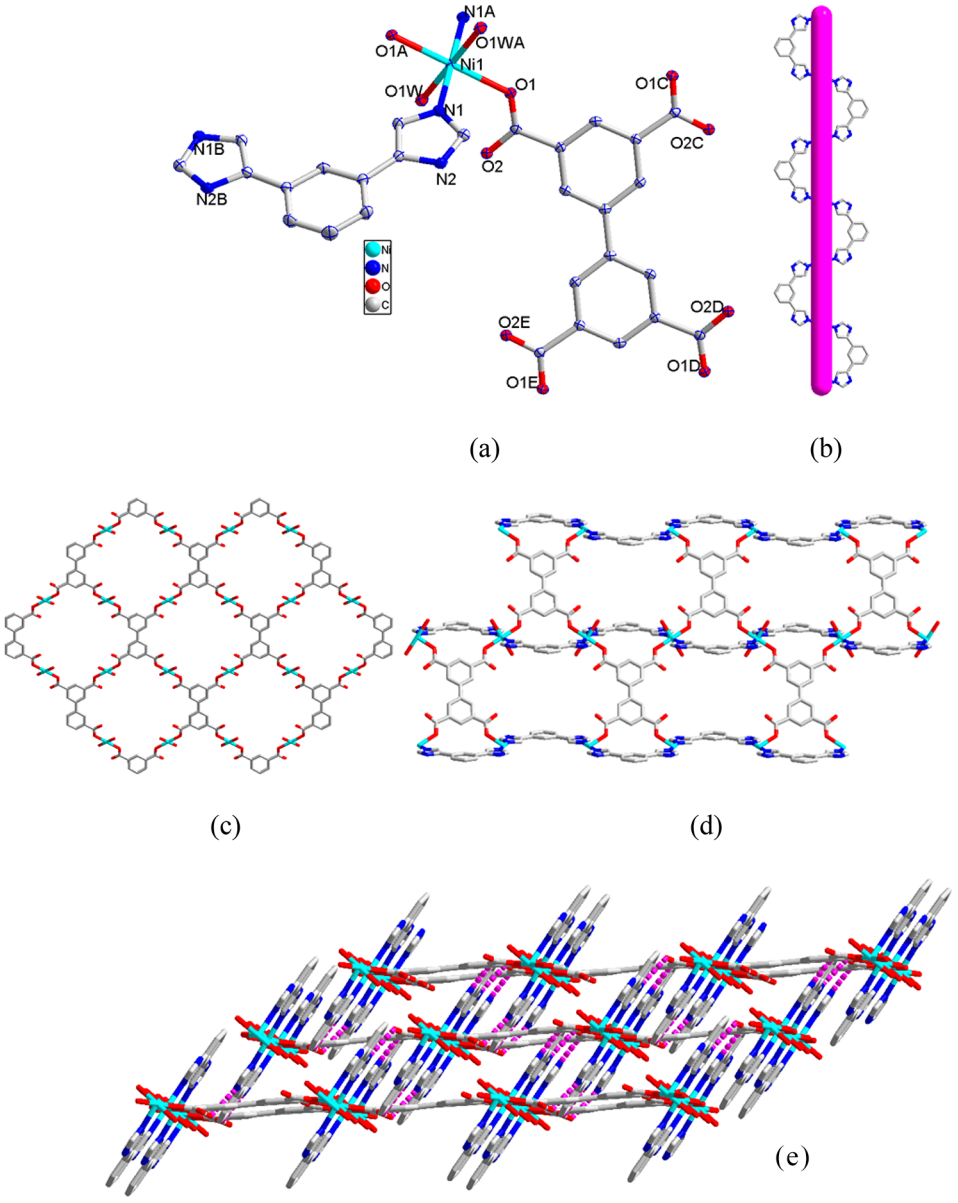

Figure 4. (a) Coordination environment of Ni(II) in **4** with the ellipsoids drawn at the 30% probability level. Hydrogen atoms and free water molecules are omitted for clarity. (b) 1D helical chain of Ni(II)-L^1 in **4**. (c) 2D structure of Ni(II)-$BPTC^{4-}$ in **4**. (d) 2D structure of **4**. (e) 3D structure of **4** with hydrogen bonds indicated by dashed lines.

the same L^1 as well as **5** and **6** with the same L^2 were achieved by using different carboxylate ligands, and **4** and **5** are 2D networks, while **2** and **6** have 3D structures. Thus, the different structures of **2** and **4** as well as **5** and **6** are ascribed to the different carboxylate ligands. In addition, ligands L^1 and L^2 also have an impact on the structures of the complexes reflected by the distinct structures of **4** and **6**. The results of this work further imply the remarkable influence of metal centers and organic ligands on the structures of the complexes.

Powder X-ray Diffraction (PXRD) and Thermal Stability. The purity for the as-synthesized samples was ensured by PXRD measurements, and the results are provided in Figure S1. Each as-synthesized sample gives a consistent PXRD pattern with the corresponding simulated one, implying the pure phase of **1**−**6**.

Thermogravimetric analyses (TGA) were employed to check the thermal stabilities of **1**−**6**, and the TG curves are given in Figure S2. MOF **1** displays a weight loss of 11.05% before 115 °C corresponding to the release of DMF (calcd 11.21%), and the residue is stable up to about 300 °C. In the case of **2**, a weight loss of 5.71% was detected in the temperature range of 30−230 °C, which is ascribed to the loss of coordinated aqua molecules (calcd 5.83%). The framework of **2** collapses from about 400 °C. For **3**, a weight of loss of 2.06% was found before 165 °C due to the removal of aqua molecule (calcd 1.94%), and further weight loss starts from about 320 °C. Complex **4** loses its 8.02% weight in the temperature range of 30−130 °C, due to the departure of the coordinated water molecules (calcd 7.69%), and further weight loss was observed at about 340 °C, corresponding to the collapse of the framework. The TG curve of **5** ensures a weight loss is 3.17% from the room temperature to 210 °C, owing to the escape of μ_2-O and coordinated water molecules (calcd 3.37%), and further loss of the organic ligands was observed at about 410 °C. In the case of **6**, a weight loss of 9.72% from 30 to 150 °C is attributed to loss of free and coordinated water molecules (calcd 9.95%), and the residue is stable up to about 360 °C.

DOI: 10.1021/acs.cgd.7b01572
Cryst. Growth Des. 2018, 18, 1136−1146

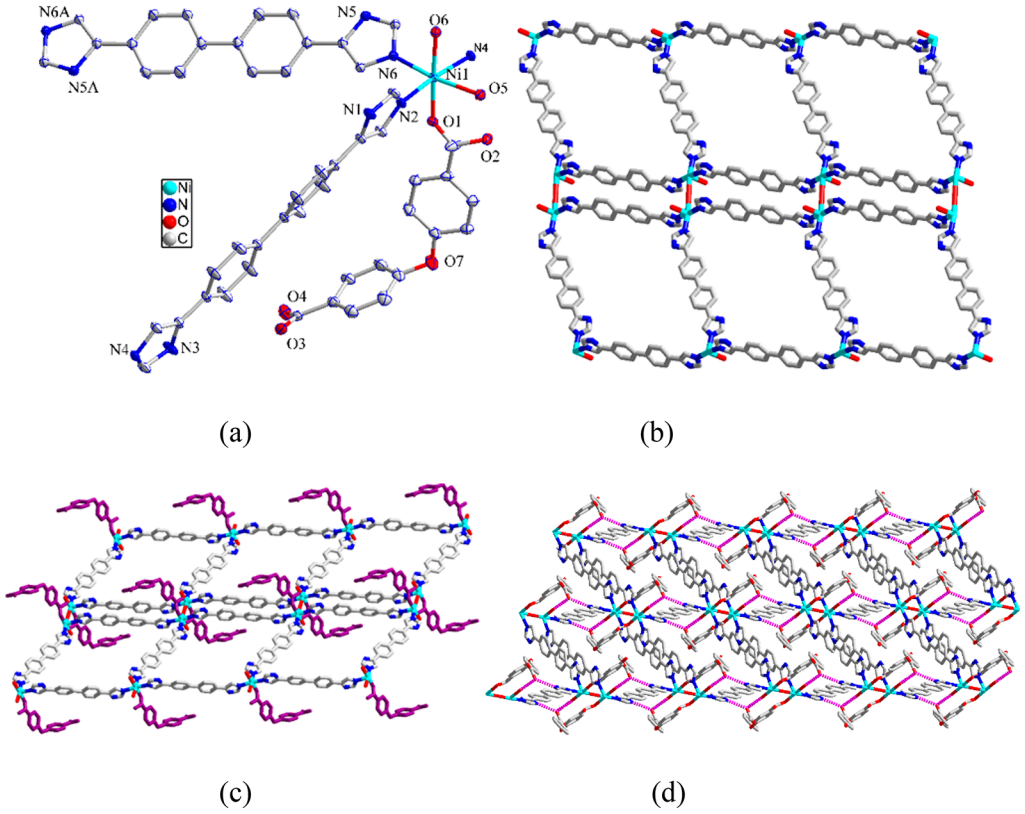

Figure 5. (a) Coordination environment of Ni(II) in **5** with the ellipsoids drawn at the 30% probability level. Hydrogen atoms and free water molecules are omitted for clarity. (b) 2D structure of Ni(II)-L^2 in **5**. (c) 2D structure of **5**. (d) 3D structure of **5** with hydrogen bonds indicated by dashed lines.

Adsorption Property. Among **1**−**6**, only **6** has a porous structure from structural analysis and stable framework after the removal of solvent molecules ensured by TG and PXRD data (Figures S1 and S2), encouraging us to examine its adsorption property. As shown in Figure 7, the activated **6** exhibits selectively adsorption of CO_2 over N_2 and selectively adsorbs H_2O over MeOH and EtOH. The uptake values for adsorption of CO_2 at 195 K and 1 atm and for H_2O at 298 K and 1 atm are 36.96 $cm^3 \cdot g^{-1}$ and 195.1 $cm^3 \cdot g^{-1}$ (156.8 $mg \cdot g^{-1}$), respectively. The selectively adsorption of CO_2 and H_2O may be ascribed to the different molecular sizes since CO_2 and H_2O have smaller kinetic diameters compared to those of N_2 and MeOH, EtOH, respectively.[18,19] The large adsorption hysteresis in sorption profiles of **6** implies the existence of strong adsorbent−adsorbate interactions.[20,21]

Photoluminescence Property. MOFs with d^{10} metal centers show luminescent properties with potential for luminescent materials.[22,23] Accordingly, the solid-state luminescent emission spectra of L^1, H_2oba, H_3BPT, **1** and **3** were collected at room temperature. Intense emission was observed with a peak at 381 nm (λ_{ex} = 335 nm) for L^1 (Figure 8), while H_2oba and H_3BPT exhibit relatively weak emissions at 330 nm (λ_{ex} = 295 nm) and 348 nm (λ_{ex} = 313 nm) (Figure S3), respectively. MOFs **1** and **3** give emissions at 342 nm (λ_{ex} = 300 nm) and 352 nm (λex = 300 nm) (Figure 8), respectively. Compared with the emission of free H_2oba, H_3BPT, and L^1 ligands, the different emissions of **1** and **3** are considered to be originated from the coordination of the ligands to the metal centers.

Sensing Small Organic Molecules. To evaluate the sensing property of **1** and **3** for small organic molecules, **1** and **3** were immersed in different organic solvents for luminescence measurements. The results clearly show the solvent-dependent emission intensities of **1** and **3** (Figure 9). Among the tested organic solvents, the stable suspension of **1** and **3** in DMF showed the strongest emission, while acetone gave the most significant quenching effect. Therefore, DMF was utilized as the suspension medium for the fluorescence sensing experiments. The quenching behavior of the acetone molecule might be ascribed to the interaction between the "C═O" group of acetone and the framework of **1** and **3**.[4,24]

To further investigate the quenching effect of acetone on the luminescence intensity, MOFs **1** and **3** were dispersed in DMF, and then acetone was added gradually to survey the emission variation. As shown in Figure 10, the fluorescence intensity of **1** and **3** decreases with the addition of acetone and almost disappeared at the acetone amount of 27 μL for **1** and 24 μL for **3**. The linear relation of decreasing trend of the fluorescence intensity for **1** and **3** vs the volume ratio of acetone in DMF suggests a diffusion controlled process (Figure 11). In addition, the Stern−Volmer equation, $(I_0/I) = K_{sv}[M] + 1$, was employed to estimate the quenching constant (K_{sv}). I_0 and I are the luminescence intensities of **1** and **3** dispersed in DMF without and with addition of acetone, respectively, and [M] is the molar concentration of acetone.[25,26] The Stern−Volmer plot for acetone is typically linear at low concentrations, and the K_{sv} values are found to be 1.169 M^{-1} for **1** and 0.7006 M^{-1} for **3** (Figure 12). The high sensitivity and selectivity of the fluorescence response of **1** and **3** to acetone show that they could be used as chemical sensors for acetone.

Luminescent Sensing of Fe^{3+}. **1** and **3** were also investigated as a luminescent sensor for the detection of metal ions. The as-synthesized sample of **1** or **3** (2 mg) was immersed in

DOI: 10.1021/acs.cgd.7b01572
Cryst. Growth Des. 2018, 18, 1136−1146

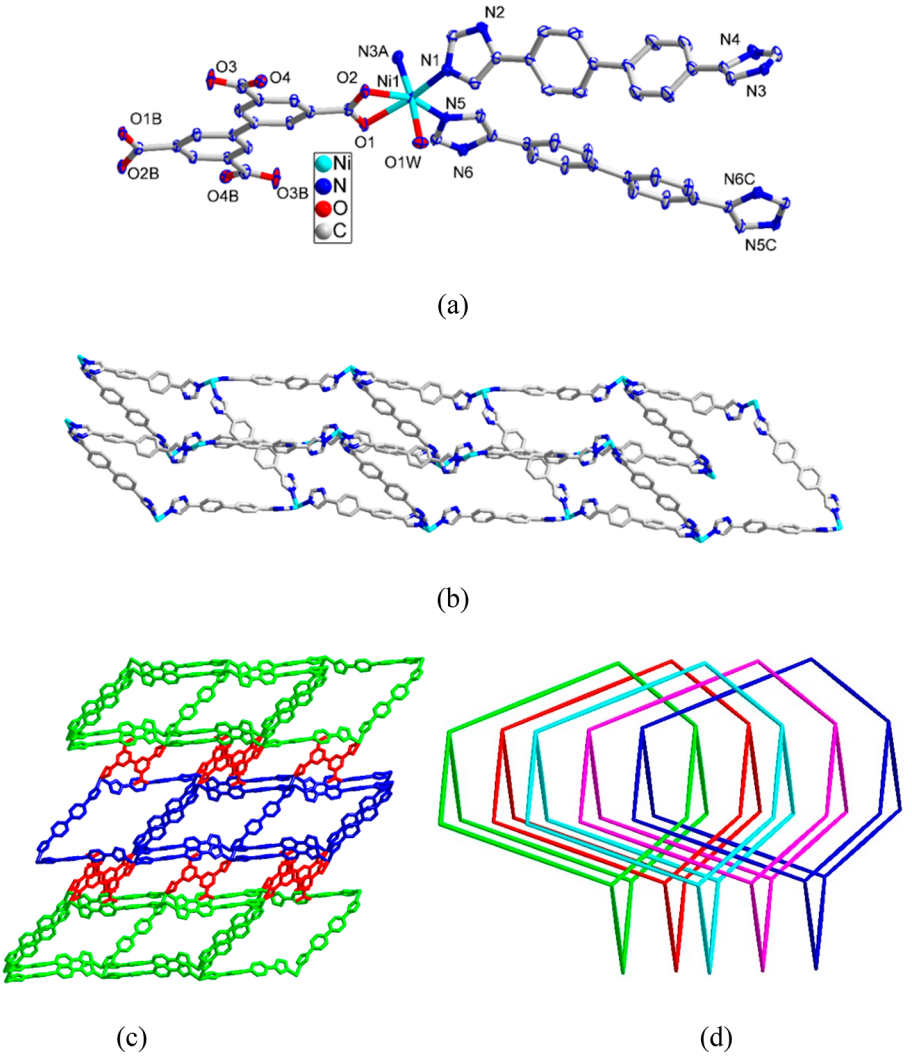

Figure 6. (a) Coordination environment of Ni(II) in **6** with the ellipsoids drawn at the 30% probability level. Hydrogen atoms and free water molecules are omitted for clarity. (b) 2D structure of Ni(II)-L^2 in **6**. (c) 3D structure of **6**. (d) Topology of **6**.

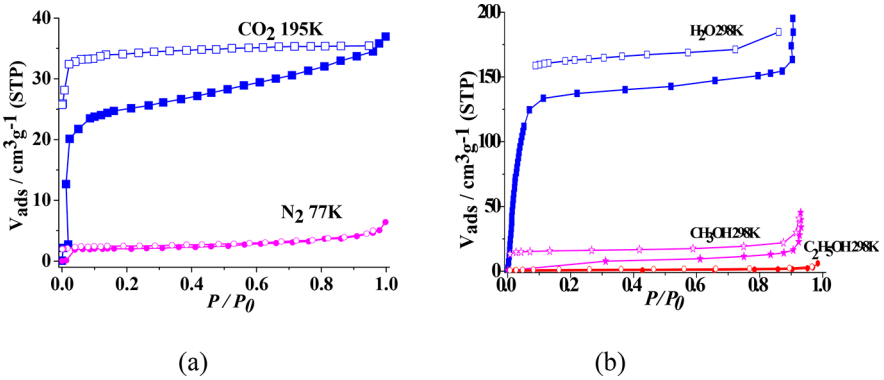

Figure 7. (a) N_2 at 77 K and CO_2 at 195 K sorption isotherms for activated **6**. (b) H_2O, MeOH, and EtOH at 298 K sorption isotherms for activated **6**.

DMF solution containing various $M(NO_3)_x$ with a concentration of [M] = 10^{-3} mol/L (M = K^+, Li^+, Na^+, Ni^{2+}, Co^{2+}, Zn^{2+}, Cu^{2+}, Cd^{2+}, Mg^{2+}, Al^{3+}, Cr^{3+}, and Fe^{3+}) to from stable suspension. As shown in Figure 13, the luminescence intensity of **1** and **3** suspension reduces to almost zero with the addition of Fe^{3+}, suggesting that they are almost quenched and exhibit high selectivity for Fe^{3+} sensing.

To estimate the detection limit of **1** and **3** as a Fe^{3+} probe, the luminescence intensities of Fe(III)-incorporated **1** and **3** were measured with different concentrations of Fe^{3+}. As depicted in Figure 14, the luminescence intensity gradually decreases with an increase of Fe^{3+} content. When Fe^{3+} concentration increased to ca. 760 μL for **1** and ca. 500 μL for **3**, the quenching efficiency reached nearly 100%. To evaluate the luminescence quenching efficiency, quenching coefficients were calculated. As illustrated in the Stern−Volmer plots of **1** and **3** at low concentrations (Figure 15), the K_{sv} values of **1** and **3** are 2.69 × 10^4 M^{-1} and 3.38 × 10^4 M^{-1}, respectively. From the slope and standard

DOI: 10.1021/acs.cgd.7b01572
Cryst. Growth Des. 2018, 18, 1136−1146

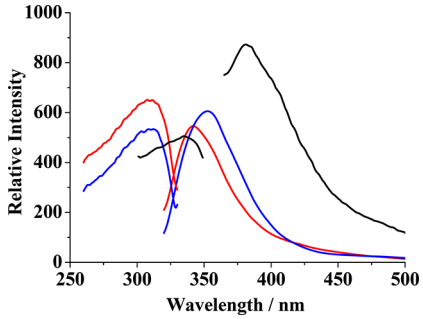

Figure 8. Excitation (left) and emission (right) spectra of **1** (red), **3** (blue), and L^1 (black) in the solid state at room temperature.

error of the fitting lines, the detection limits are found to be 103 ppb for **1** and 72 ppb for **3** according to the equation $3\sigma/k$ (σ: standard error; k: slope), which are comparable to those for the reported MOFs for sensing Fe^{3+}.[27−30] It implies that **1** and **3** can selectively sense Fe^{3+} ions.

To examine the sensing mechanism of **1** and **3** toward acetone and Fe^{3+}, UV/vis spectra of **1**, **3**, acetone and Fe^{3+} were measured. It can be seen that acetone and Fe^{3+} have better UV/vis absorption in a wide range than **1** and **3**, covering the range of absorption of **1** and **3** (Figure S4). The results imply that the UV/vis absorption of acetone as well as Fe^{3+} upon excitation may prevent the absorption of **1** and **3**, and result in the decrease or quenching of the luminescence.[15,31]

CONCLUSIONS

In summary, we have successfully fabricated six new MOFs based on rigid 1*H*-imidazol-4-yl containing and varied carboxylate

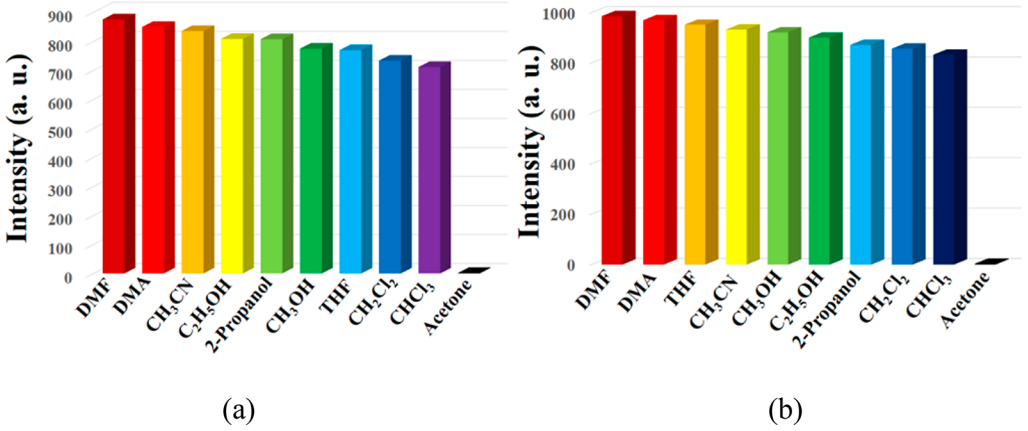

Figure 9. Photoluminescence intensities introduced into varied pure solvent when excited at 300 nm for **1** (a) and **3** (b).

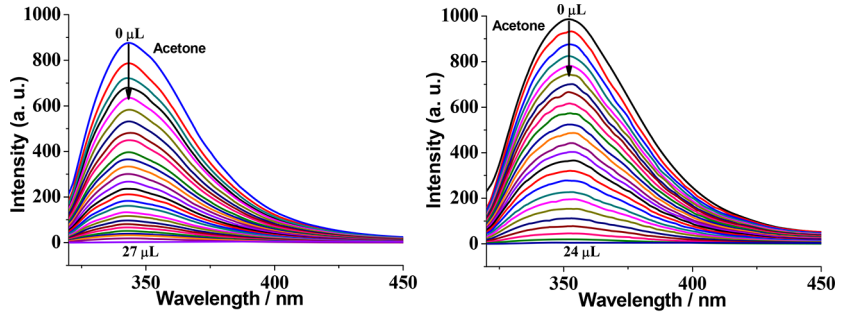

Figure 10. Photoluminescence spectra of the dispersed **1** (a) and **3** (b) in DMF in the presence of varied contents of the acetone (excited at 300 nm).

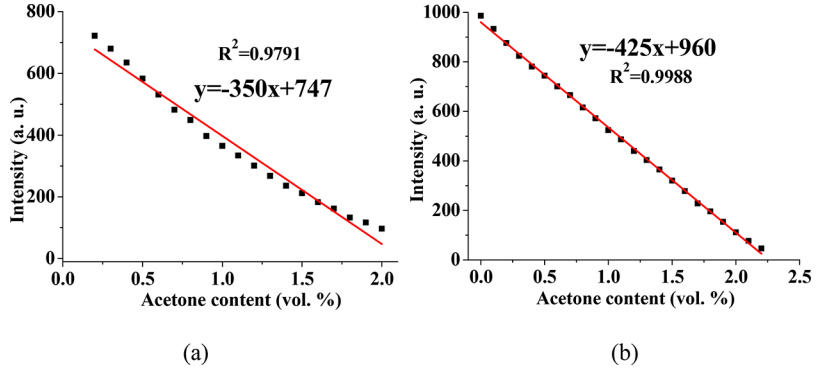

Figure 11. Photoluminescence intensities of **1** (a) and **3** (b) in DMF as a function of acetone content (excited at 300 nm).

DOI: 10.1021/acs.cgd.7b01572
Cryst. Growth Des. 2018, 18, 1136−1146

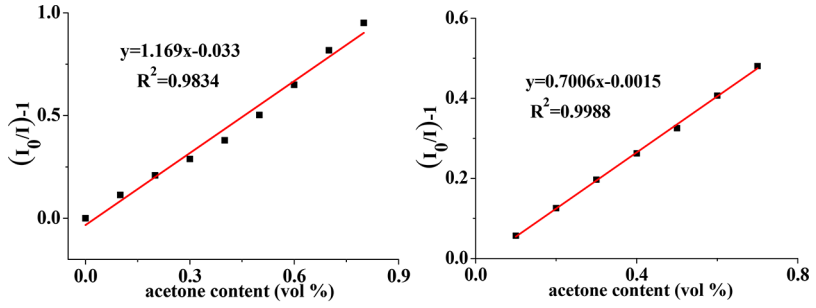

(a) (b)

Figure 12. Stern–Volmer plots of **1** (a) and **3** (b) for acetone.

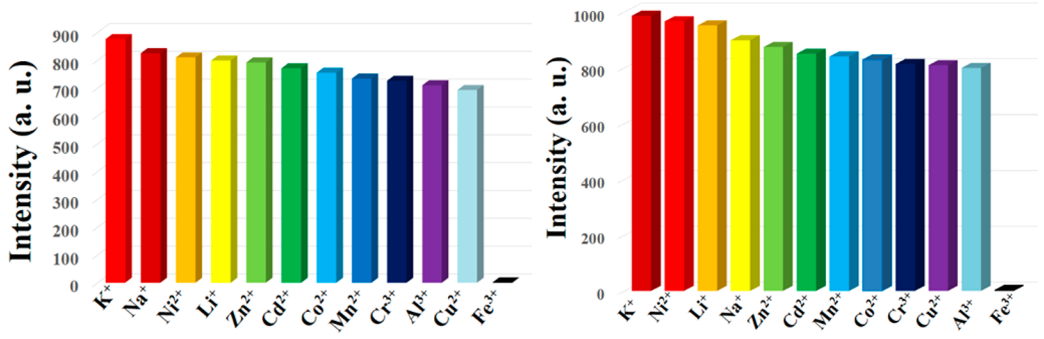

(a) (b)

Figure 13. Photoluminescence intensities introduced into different metal ions dissolved in DMF when excited at 300 nm for **1** (a) and **3** (b).

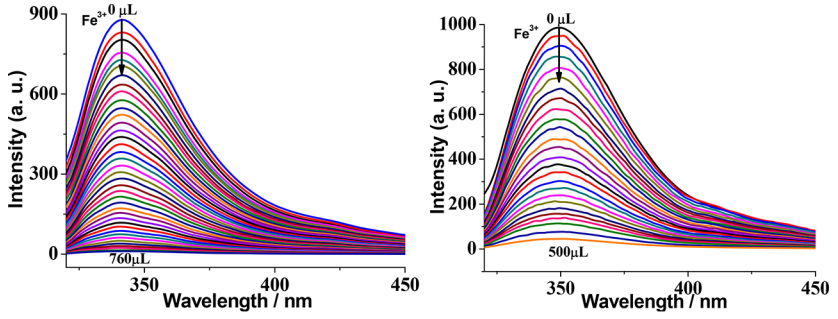

(a) (b)

Figure 14. Photoluminescence spectra of the dispersed **1** (a) and **3** (b) in DMF in the presence of various contents of the Fe(III) (excited at 300 nm).

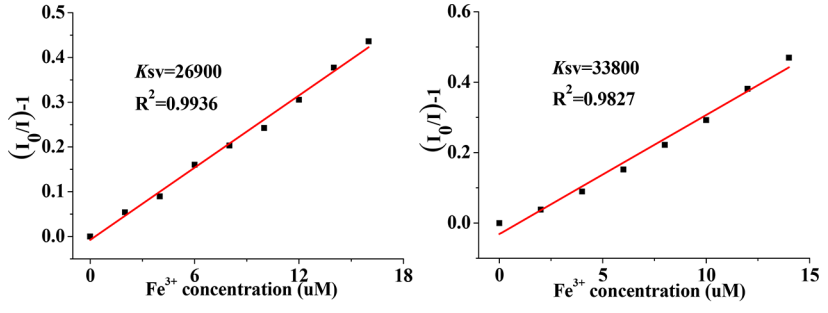

(a) (b)

Figure 15. Stern–Volmer plot of **1** (a) and **3** (b) for Fe(III).

ligands via hydro- and solvothermal reactions. The results show that the structural diversification of the frameworks may be attributed to coordination behavior of the metal centers and coordination mode of the ligands. In addition, MOFs **1** and **3**

DOI: 10.1021/acs.cgd.7b01572
Cryst. Growth Des. 2018, 18, 1136–1146

can serve as a multiresponsive luminescent sensor, which is capable of detecting acetone molecules and Fe^{3+} ions. Moreover, **6** exhibits selectively adsorption of CO_2 over N_2.

■ ASSOCIATED CONTENT

Supporting Information

The Supporting Information is available free of charge on the ACS Publications website at DOI: 10.1021/acs.cgd.7b01572.

Experimental Section, tables for selected bond lengths and angles, hydrogen bonding and schemes for coordination modes of carboxylate ligands, structure figures, PXRD patterns and TG (PDF)

Accession Codes

CCDC 1580273−1580278 contain the supplementary crystallographic data for this paper. These data can be obtained free of charge via www.ccdc.cam.ac.uk/data_request/cif, or by emailing data_request@ccdc.cam.ac.uk, or by contacting The Cambridge Crystallographic Data Centre, 12 Union Road, Cambridge CB2 1EZ, UK; fax: +44 1223 336033.

■ AUTHOR INFORMATION

Corresponding Author

*Tel: +86 25 89683485. E-mail: sunwy@nju.edu.cn.

ORCID

Qing-Yi Lu: 0000-0002-6160-9499

Wei-Yin Sun: 0000-0001-8966-9728

Notes

The authors declare no competing financial interest.

■ ACKNOWLEDGMENTS

We gratefully acknowledge the National Natural Science Foundation of China (Grant Nos. 21331002 and 21573106) and the National Basic Research Program of China (Grant No. 2017YFA0303500) for financial support of this work. The authors extend their appreciation to the International Scientific Partnership Program ISPP at King Saud University for funding this research work through ISPP#0090. This work was also supported by a project funded by the Priority Academic Program Development of Jiangsu Higher Education Institutions.

■ REFERENCES

(1) Zhou, H.-C.; Long, J.-R.; Yaghi, O.-M. *Chem. Rev.* **2012**, *112*, 673−674.

(2) Lee, J.-Y.; Farha, O.-K.; Roberts, J.; Scheidt, K.-A.; Nguyen, S.-T.; Hupp, J.-T. *Chem. Soc. Rev.* **2009**, *38*, 1450−1459.

(3) Seoane, B.; Coronas, J.; Gascon, I.; Benavides, M.-E.; Karvan, O.; Caro, J.; Kapteijn, F.; Gascon, J. *Chem. Soc. Rev.* **2015**, *44*, 2421−2454.

(4) Liu, Z.-Q.; Huang, Y.-Q.; Sun, W.-Y. *Chin. J. Inorg. Chem.* **2017**, *33*, 1959−1969.

(5) He, C.-B.; Liu, D.-M.; Lin, W.-B. *Chem. Rev.* **2015**, *115*, 11079−11108.

(6) Jiang, H.-L.; Feng, D.-W.; Liu, T.-F.; Li, J.-R.; Zhou, H.-C. *J. Am. Chem. Soc.* **2012**, *134*, 14690−14693.

(7) Guo, M.; Sun, Z.-M. *J. Mater. Chem.* **2012**, *22*, 15939−15946.

(8) Busse, M.; Andrews, P.-C.; Junk, P.-C. *Eur. J. Inorg. Chem.* **2012**, *2012*, 1061−1071.

(9) Tanabe, K.-K.; Cohen, S.-M. *Chem. Soc. Rev.* **2011**, *40*, 498−519.

(10) Ren, Y.-X.; Zheng, X.-J.; Li, L.-C.; Yuan, D.-Q.; An, M.; Jin, L.-P. *Inorg. Chem.* **2014**, *53*, 12234−12236.

(11) Colombo, V.; Montoro, C.; Maspero, A.; Palmisano, G.; Masciocchi, N.; Galli, S.; Barea, E.; Navarro, J. A. R. *J. Am. Chem. Soc.* **2012**, *134*, 12830−12843.

(12) Liu, Z.-Q.; Zhao, Y.; Deng, Y.; Zhang, X.-D.; Kang, Y.-S.; Lu, Q.-Y.; Sun, W.-Y. *Sens. Actuators, B* **2017**, *250*, 179−188.

(13) Deng, Y.; Yao, Z.-Y.; Wang, P.; Zhao, Y.; Kang, Y.-S.; Sun, W.-Y. *Sens. Actuators, B* **2017**, *244*, 114−123.

(14) Liu, Z.-Q.; Zhao, Y.; Wang, P.; Kang, Y.-S.; Azam, M.; Al-Resayes, S.-I.; Liu, X.-H.; Lu, Q.-Y.; Sun, W.-Y. *Dalton Trans.* **2017**, *46*, 9022−9029.

(15) Zhao, D.; Liu, X.-H.; Zhao, Y.; Wang, P.; Liu, Y.; Azam, M.; Al-Resayes, S.-I.; Lu, Y.; Sun, W.-Y. *J. Mater. Chem. A* **2017**, *5*, 15797−15807.

(16) Blatov, V.-A. *IUCr Comp Comm Newsl.* **2006**, *7*, 4.

(17) Blatov, V.-A. *TOPOS, A Multipurpose Crystallochemical Analysis with the Program Package Topos*; Samara State University: Russia, 2009.

(18) Li, Y.-L.; Zhao, Y.; Kang, Y.-S.; Liu, X.-H.; Sun, W.-Y. *Cryst. Growth Des.* **2016**, *16*, 7112−7123.

(19) Hua, J.-A.; Zhao, Y.; Liu, Q.; Zhao, D.; Chen, K.; Sun, W.-Y. *CrystEngComm* **2014**, *16*, 7536−7546.

(20) Luo, L.; Wang, P.; Liu, Q.; Okamura, T.; Lv, G.-C.; Lu, Y.; Sun, W.-Y. *Microporous Mesoporous Mater.* **2016**, *219*, 199−208.

(21) Peterson, V.-K.; Southon, P.-D.; Halder, G.-J.; Price, D.-J.; Bevitt, J.-J.; Kepert, C.-J. *Chem. Mater.* **2014**, *26*, 4712−4723.

(22) Liu, X.-J.; Zhang, Y.-H.; Chang, Z.; Li, A.-L.; Tian, D.; Yao, Z.-Q.; Jia, Y.-Y.; Bu, X.-H. *Inorg. Chem.* **2016**, *55*, 7326−7328.

(23) Chen, D.-M.; Tian, J.-Y.; Chen, M.; Liu, C.-S.; Du, M. *ACS Appl. Mater. Interfaces* **2016**, *8*, 18043−18050.

(24) Ma, C.; Jiao, C.-Q.; Sun, Z.-G.; Zhu, Y.-Y.; Zhang, X.-W.; Wang, M.-L.; Yang, D.; Zhao, Z.; Li, H.-Y.; Xing, B. *RSC Adv.* **2015**, *5*, 79041−79049.

(25) Yang, Y.; Chen, L.; Jiang, F.-L.; Wan, X.-Y.; Yu, M.-X.; Cao, Z.; Jing, T.; Hong, M.-C. *J. Mater. Chem. C* **2017**, *5*, 4511−4519.

(26) Rachuri, Y.; Parmar, B.; Bisht, K.-K.; Suresh, E. *Dalton Trans.* **2017**, *46*, 3623−3630.

(27) Wang, J.; Jiang, M.; Yan, L.; Peng, R.; Huangfu, M.-J.; Guo, X.-X.; Li, Y.; Wu, P.-Y. *Inorg. Chem.* **2016**, *55*, 12660−12668.

(28) Li, L.; Chen, Q.; Niu, Z.-G.; Zhou, X.-H.; Yang, T.; Huang, W. *J. Mater. Chem. C* **2016**, *4*, 1900−1905.

(29) Wang, B.; Yang, Q.; Guo, C.; Sun, Y.-X.; Xie, L.-H.; Li, J.-R. *ACS Appl. Mater. Interfaces* **2017**, *9*, 10286−10295.

(30) Zhao, X.-L.; Tian, D.; Gao, Q.; Sun, H.-W.; Xu, J.; Bu, X.-H. *Dalton Trans.* **2016**, *45*, 1040−1046.

(31) Liu, Z.-Q.; Zhao, Y.; Zhang, X.-D.; Kang, Y.-S.; Lu, Q.-Y.; Azam, M.; Al-Resayes, S.-I.; Sun, W.-Y. *Dalton Trans.* **2017**, *46*, 13943−13951.

DOI: 10.1021/acs.cgd.7b01572
Cryst. Growth Des. 2018, 18, 1136−1146